

Seasonal variability of ocean circulation near the Dotson Ice Shelf, Antarctica

Hee Won Yang

Korea Polar Research Institute

Tae-Wan Kim (✉ twkim@kopri.re.kr)

Korea Polar Research Institute <https://orcid.org/0000-0001-5257-7256>

Pierre Dutrioux

British Antarctic Survey <https://orcid.org/0000-0002-8066-934X>

A. K. Wahlin

University of Gothenburg <https://orcid.org/0000-0003-1799-6476>

Adrian Jenkins

Northumbria University <https://orcid.org/0000-0002-9117-0616>

Ho Kyung Ha

Inha University <https://orcid.org/0000-0002-8274-9247>

Chang-Sin Kim

National Institute of Fisheries Science <https://orcid.org/0000-0003-3026-3285>

Kyoung-Ho Cho

Korea Polar Research Institute (KOPRI) <https://orcid.org/0000-0001-5527-5851>

Taewook Park

Korea Polar Research Institute

SangHoon Lee

Korea Polar Research Institute

Yang-Ki Cho

Seoul National University

Article

Keywords: Dotson Ice Shelf, ocean circulation, melting, climate

Posted Date: February 2nd, 2021

DOI: <https://doi.org/10.21203/rs.3.rs-152149/v1>

License:   This work is licensed under a Creative Commons Attribution 4.0 International License.

[Read Full License](#)

Version of Record: A version of this preprint was published at Nature Communications on March 3rd, 2022. See the published version at <https://doi.org/10.1038/s41467-022-28751-5>.

Seasonal variability of ocean circulation near the Dotson Ice Shelf, Antarctica

H. W. Yang^{1,8}, T.-W. Kim^{1*}, Pierre Dutrieux^{2,3}, A. K. Wåhlin⁴, Adrian Jenkins⁵, H. K. Ha⁶, C. S. Kim⁷, K.-H. Cho¹, T. Park¹, S. H. Lee¹ & Y. K. Cho⁸

¹ Korea Polar Research Institute, Incheon 21990 South Korea

² British Antarctic Survey, Natural Environment Research Council, Cambridge CB3 0ET, U.K.

³ Lamont-Doherty Earth Observatory of Columbia University, Palisades, NY 10964, U.S.A.

⁴ Department of Marine Sciences, University of Gothenburg, Gothenburg, Sweden

⁵ University of Northumbria, Newcastle upon Tyne NE1 8QH, U.K.

⁶ Department of Ocean Sciences, Inha University, Incheon 22212 South Korea

⁷ National Institute of Fisheries Science, Busan 46083 South Korea

⁸ School of Earth and Environmental Sciences/Research Institute of Oceanography, Seoul National University, Seoul 08826, South Korea

*Corresponding author: Tae-Wan Kim

Korea Polar Research Institute, Incheon 21990, South Korea

Tel: +82-32-760-5338; Fax: +82-32-760-5399

E-mail addresses: twkim@kopri.re.kr (T.-W. Kim)

Abstract

Recent rapid thinning of West Antarctic ice shelves are believed to be caused by intrusions of warm deep water that induce basal melting and seaward meltwater export. Dotson Ice Shelf has a high basal melt rate due to southward ocean heat transport in the Dotson-Getz Trough. We deployed three bottom-moored instrument arrays along the ice shelf calving front, obtaining continuous records of temperature, salinity, and current velocity throughout 2014 and 2015. Southward deep water velocities were highest along the eastern channel slope, while northward outflows of freshened ice shelf meltwater spread at intermediate depth above the western slope. Inflow warm water along the eastern slope into the sub-Dotson cavity reached a maximum of 182 MW m^{-1} in Summer, 3.5 times larger than the autumn/winter values of 51 MW m^{-1} . The inflow correlated with the local ocean surface stress curl. At the western slope meltwater outflows were strongest during autumn and weakest in spring, following the warm influx along the eastern slope with a ~2-3 months delay. Ocean circulation near Dotson Ice Shelf, affected by sea ice distribution and wind, appears to be a significant control on the inflow of warm water and subsequent ice shelf melting on seasonal time-scales.

Introduction

Glacier flow in West Antarctica has been increasing^{1,2,3,4,5}, with a noticeable impact on global sea level rise^{6,7}. The cause for the recent flow increase is believed to be the thinning of the buttressing ice shelves⁸.

Ice shelf melting is highest in the Amundsen Sea, where deep-draft ice is more readily accessible by warm and salty modified Circumpolar Deep Water (CDW) that intrudes onto its continental shelf^{9,10,11,12,13,14,15}. Prior research has indicated a seasonal pattern to such intrusions due to changes in sea ice and wind distribution^{16,17}. The Dotson Ice Shelf (DIS) buttresses the Kohler and Smith Glaciers and has thinned by 2.6 m yr⁻¹ between 1994 and 2012, a rate intermediate between the adjacent Crosson and Getz ice shelves⁵, but with a higher melting to calving ratio^{2,3}. Understanding seawater circulation near the ice shelf is important for determining how changes in oceanic heat transport affect its basal melting^{18,19}. A stronger influx of mCDW (slightly cooler and fresher water compared with CDW) that has access to the ice shelf base will accelerate melting, leading to mass loss in its glaciers. However, the temporal variability of that circulation, and how it propagates into the cavity beneath the ice shelves, is not yet well known. In this study, we investigate temporal and spatial variations in ocean circulation and heat transport to and from the sub-DIS cavity and look into associated forcing mechanisms.

Results

Several field surveys using icebreakers have been conducted since 1994 to identify variability in the mCDW intrusion rate and its circulation in the Amundsen Sea, mostly during the austral summer²⁰. Time series based on moored instrumentation is more rare. In January 2014, three bottom-moored arrays were deployed from the South Korean icebreaker Araon along the DIS calving front to measure the variability of temperature, salinity, and currents (K4, K3, and K5 in Fig. 1a). These moorings were located at the center of the Dotson-Getz Trough (DGT) and on its eastern and western slopes, 2–3 km away from the calving front. The eastern and western moorings were expected to measure mCDW inflows and meltwater outflows, respectively, and their variability. All but one Acoustic Doppler Current Profiler (ADCP) recorded successfully for two years, while one ADCP measuring bottom current velocity on the eastern mooring provided a one-year record (Supplementary Table 1, Supplementary Fig. 1).

South-westward currents predominated near the bottom on the eastern side throughout the record, with an average current speed near 17 cm s⁻¹ at 680 m (Fig. 1a). Away from the seabed the current was somewhat weaker and veered westward. Near the western flank, weak south-eastward flows (around 1 cm s⁻¹) were measured at 700 m (Fig. 1b). The current direction gradually turned eastward at shallower levels, with average current speed reaching 1.2 cm s⁻¹ at 420 m (Fig. 1a). Warm and salty mCDW (2 °C higher than the freezing point) was found flowing towards DIS at the eastern flank below 700 m (Fig. 1c and d), with averages temperature and salinity for two years at 747 m near the seabed being 0.3 °C

and 34.5, respectively. In contrast, the outflows of relatively cold and freshwater was found above 500 m near the western flank (Fig. 1b and e).

The predominantly south-westward flow on the eastern flank (Fig. 2a and b) displayed large, depth-independent seasonal and intra-seasonal variability. Near the bottom (680 m), the southward (towards the ice shelf cavity) flow reached a maximum of 20 cm s^{-1} in January 2014 and a minimum of 12 cm s^{-1} in May. The southward component decreased gradually at mid-depth, but its periodicity remained the same in the whole water column. At the 400 m depth, the observed maximum southward component was 9 cm s^{-1} in January 2016, and a northward component of 2 cm s^{-1} was measured in April 2015. Vertical meridional current shear increased toward the bottom but the remained nearly constant during the measured period. It is concluded that the seasonality of the southward component is a barotropic process, and that the baroclinic component (indicated by the vertical shear) does not significantly affect the temporal variability of the southward flow.

In summer, the strong barotropic southward flows drive a increase of salinity in front of the DIS (Supplementary Fig. 2) because the salinity is relatively low in front of the DIS due to the strong downwelling²¹. Salinity at mid-depths (above 500 m) varied seasonally near the eastern and central front, as shown by the 34.2 isohaline, rising from ~ 450 m in early spring to ~ 300 m in early summer and deepening 450–500 m for the rest of the year. The salinity difference between the eastern and central front was negligibly small in the mid-depth. Nearer the seabed there was no distinct seasonal variability of the salinity, but a noticeable eastward gradient increased in association with intrusions of mCDW along the eastern flank. The salinity at 750 m was above 34.5 on the eastern side, 34.4 in the center, and 34.35–34.4 on the western side. Such a salinity gradient is associated with an increase of southward current shear near the bottom.

To estimate the effect of barotropic component on the variability of the southward current near the eastern side of DIS front, the Ocean Surface Stress Curl (OSSC, Fig. 2c) was calculated from sea ice motion and wind using the ice-ocean drag coefficient (see Methods and Supplementary Fig. 5). On the eastern flank the OSSC was on average higher than on the western, varied substantially, and correlated ($r = 0.64$, with a 35 day lag) with the vertically averaged southward velocity (Fig 2d). We interpret this statistically significant relationship as an indication that higher OSSC over the eastern flank creates a zonal barotropic pressure gradient driving a southward velocity. During summer, the OSSC increases due to strong southeasterly winds over the open sea and during winter it decreases when the wind stress and currents are weakened by the sea ice cover (Fig. 2c). The relatively high OSSC near the DIS can also induce a barotropic pressure gradients in the meridional direction, which may similarly drive the

strongly barotropic westward Antarctic coastal current at mid-depth (Fig. 2a). The westward current component decreases with depth due to the eastward baroclinic shear caused by the local down-welling associated with high OSSC near the ice shelf front.

On the western flank of the ice shelf front, the seasonal variation, most prominent in mid-depth, had a range about half that of the eastern side bottom (Fig. 3a and b). Near the bottom, near-constant weak southeastward currents were observed during the entire record. The meridional current component shifted between northward in fall and southward in spring (Fig. 3b) and the current velocities were generally smaller compared to the eastern flank. In both 2014 and 2015, the highest northward velocity were 2.9 cm s^{-1} and 2.5 cm s^{-1} in April and the highest southward velocity were 2.5 cm s^{-1} in early October. The eastward current component had maximum in winter, 4.2 cm s^{-1} and 4.9 cm s^{-1} at 420 m depth in July (Fig. 3a), and was almost constant close to 2 cm s^{-1} in summer. The occurrence of eastern flow in the winter coincides with a decrease of OSSC at the western side of DIS front (Fig. 3c), and an associated local drop in sea level height, intensifying the eastward barotropic current in the entire water column. However, the upwelling accompanied by negative OSSC generates a westward baroclinic current that countervails the eastward barotropic current at a deeper depth.

During all seasons, there was a weak southward flow present near the bottom throughout the record (Fig. 3b), presumably driven by the cross-front salinity distribution which increased toward the eastern side of DIS due to the inflow of mCDW. In the middle layer, the northward current component had a seasonal maximum in autumn, both years, coinciding with maximums of the meltwater fraction (Fig. 3 b and d). The meltwater outflows occurred mainly in the middle layer and may be significant enough over long timescales to influence the general ocean circulation²¹. Since the mooring did not cover the upper water column, it is believed that much of the meltwater outflow remained undetected. However, the signal is sufficiently strong to identify the seasonal variation of the outflow. We observe a seasonal variation of the meltwater fraction (Fig. 3d, Methods), with maximum exceeding 1% in April for 275 m depth in both years. The seasonal phase of the maximum meltwater fraction is delayed gradually toward the bottom, with the maximum at 575 m (0.45%) appearing in July. In contrast, the minimum meltwater fraction appeared in early October/September both year for the whole water column.

A decrease of vertically integrated density along the western side of the ice front by an inflow of meltwater during autumn can lead to local sea-level rise and increase in the northward barotropic current. This is illustrated in Fig. 3e that shows the vertical mean northward current velocity plotted together with the upper layer meltwater fraction (correlation coefficient $r=0.76$, 99% significant level, with 16 days lag). Thus, the variability of meridional current at the western side of DIS may be influenced by

meltwater discharge. This is in contrast to the eastern side, where it is primarily OSSC that changes the velocity. At a deeper depth, the freshening by an inflow of meltwater in the water column causes the increase in the southward baroclinic current countervailed the northward barotropic current. Furthermore, the northward flows created by the freshening could affect the spread of meltwater again. Finally, the decrease of meltwater discharge in spring may weaken the stratification, enhance sea-ice production-driven deep convection, and lead to rapid reduction of upper layer meltwater fraction as vertical mixing homogenize water column.

Heat transport toward the DIS near its eastern front was estimated as a function of heat content and southward current velocity for the two years (see Methods and Fig 4). The heat transport varied between 50 and 180 MW m⁻¹, with a clear seasonal dependence, and summertime values more than threefold those of winter due to the strengthened southward velocities and highest seawater temperature near the bottom. Such a dramatic seasonal dependence is expected to have major implications for basal melt, hitherto not observed in remote sensing products and unaccounted for in time series interpretations of ice shelf monitoring. However, it is not known how much of the recorded seasonal variation that makes it into the ice shelf cavity. Recent study suggest that the barotropic current component, which is a strong contributor to the seasonal variability, is blocked at the ice front²². Nevertheless, the seasonal variability of heat transport in front of the ice shelf will be propagated to under the ice shelf because the barotropic southward flows affect the variability of isohalines and isotherms (Supplementary Figure 3), and that signal is expected propagates in the cavity. The oceanic heat transport along the eastern slope melts the DIS's base, and a fresh meltwater mixture returns to the open sea along the western slope. Meltwater fluxes on the west side seemingly follows heat transports on the east side with a 74 days lag (correlation of $r = 0.50$ on a 99% significance level, Fig. 4b). Such a significant correlation indicated that the heat transport to the ice cavity affected by the OSSC variability at the eastern slope causes the seasonal variation of meltwater discharge and northward flow at the western slope.

Using two-year mooring measurements near the ice shelf calving front, we found that heat transport towards the Dotson cavity along the eastern flank of Dotson Trough, and the meltwater discharge along the western flank, had a strong seasonal variation. The seasonality of the inflow is interpreted to be caused by local OSSC, induced by changes in sea ice and wind distribution. During autumn, increasing meltwater on the western Dotson ice flank relates to the intense summer inflow of warm mCDW along the eastern Dotson ice shelf cavity. The associated, delayed freshening due to the increase of the meltwater in turn influence the northward outflow. This finding implies that the ocean circulation and local meteorological conditions in front of the ice shelf plays an important role in regulating mCDW

inflow and the basal melting of the ice shelf. Understanding these processes is therefore likely essential for determining the long-term melting trend. It is clear that the propagation into the cavity of the seasonally varying heat transport evidenced here is potentially a major and previously unknown effect that needs further investigation, e.g. based on instrumentation inside the cavity^{15,20}.

Methods

Data collection

To monitor the temporal and spatial variation of CDW and its effect on the rapid melting of glaciers in the Amundsen Shelf, we conducted extensive oceanographic surveys 4 times from 2010 to 2016. The temporal variability and properties of mCDW and its circulation in front of the DIS were obtained from the K3, K4, and K5 moorings deployed on January 8–9 2014 and recovered on January 19–20, 2016. At each station, the current velocities were observed from dual ADCPs with upward-looking 150 kHz (K4 and K5) or 75 kHz (K3) and downward-looking 300 kHz (K3, K4, and K5) RD Instruments (RDI) (Supplementary Table 1). All ADCPs were configured in narrowband mode for optimal range. The upward-looking 150 kHz and 75 kHz ADCPs used 8 m bins and 15 min ensembles of 25 and 40 pings, respectively. The downward-looking 300 kHz ADCP used 4 m bins and 15 min ensembles of 20 pings. Unfortunately, the latter recorded velocities for only 371 and 713 days from Jan. 2014 at K4 and K5, respectively, but the other ADCPs recorded continuously during the entire observation period (Supplementary Fig. 1). The observed velocities were processed using WinADCP[®] software and the tidal signal was removed using the `t_tide` toolbox²³.

In addition, the moorings contained 8 (K4 and K5) or 12 (K3) Sea-Bird Electronics (SBE) 37-SM or 37-SMP-ODO MicroCAT sensors (Supplementary Table 1) to observe conductivity as an accuracy of 0.0003 S m^{-1} , temperature (accuracy of 0.002 K), and dissolved oxygen (accuracy of $3 \mu\text{mol kg}^{-1}$).

Heat transport and meltwater fraction calculations

The heat content (HC , J m^{-3}) at each mooring was calculated relative to the freezing point:

$$HC = \rho_0 C_p (T - T_f) \quad (1)$$

where ρ_0 is the reference seawater density (1027 kg m^{-3}); C_p is the specific heat of seawater ($3986 \text{ JK}^{-1} \text{ kg}^{-1}$); and T and T_f are seawater temperature and freezing temperature based on the salinity and pressure, respectively.

To calculate heat transport during the entire observation period from 400–680 m, velocity below 600 m depth since Jan. 2015 at K4 was estimated from the relationship between the meridional velocity of the 600 m layer and data every 20 m (620 m, 640 m, 660 m, 680 m) from Jan. 2014 to Jan. 2015:

$$V_{620} = 1.064 \times V_{600} - 2.403 \text{cms}^{-1} \quad (2.1)$$

$$V_{640} = 0.985 \times V_{600} - 5.079 \text{cms}^{-1} \quad (2.2)$$

$$V_{660} = 0.924 \times V_{600} - 7.776 \text{cms}^{-1} \quad (2.3)$$

$$V_{680} = 0.880 \times V_{600} - 10.318 \text{cms}^{-1} \quad (2.4)$$

The linear regression showed a high coefficient of determination from 0.93 to 0.64 (Supplementary Fig. 4). Heat transport in the 400–680 m layer was calculated from estimated meridional velocity and heat content:

$$Q = \int_{680}^{400} \rho_0 C_p (T - T_f) \times V dz \quad (3)$$

The outflow water from DIS was considered a mixture of winter water (WW), CDW, and ice shelf meltwater based on the assumption that the ice-seawater system was closed. This relationship was expressed by water mass (V) and properties (χ^1, χ^2)²⁴:

$$V_{cdw} + V_{ww} + V_{melt} = 1 \quad (4.1)$$

$$V_{cdw} * \chi^1_{cdw} + V_{ww} * \chi^1_{ww} + V_{melt} * \chi^1_{melt} = \chi^1_{obs} \quad (4.2)$$

$$V_{cdw} * \chi^2_{cdw} + V_{ww} * \chi^2_{ww} + V_{melt} \chi^2_{melt} = \chi^2_{obs} \quad (4.3)$$

Following the conservation equation for the above equation, the meltwater fraction (φ) was then calculated from observed in situ temperature and salinity and the end-members of ice and especially water mass^{20,25,26,27}:

$$\begin{aligned} \psi_{melt}^{T,S} &= (\chi_{melt}^T - \chi_{CDW}^T) - (\chi_{melt}^S - \chi_{CDW}^S) \left(\frac{\chi_{WW}^T - \chi_{CDW}^T}{\chi_{WW}^S - \chi_{CDW}^S} \right) \\ \psi_{mix}^{T,S} &= (\chi_{obs}^T - \chi_{CDW}^T) - (\chi_{obs}^S - \chi_{CDW}^S) \left(\frac{\chi_{WW}^T - \chi_{CDW}^T}{\chi_{WW}^S - \chi_{CDW}^S} \right) \\ \varphi &= \frac{\psi_{mix}^{T,S}}{\psi_{melt}^{T,S}} \end{aligned} \quad (5)$$

where χ^T and χ^S represent potential temperature and salinity and subscripts *melt*, *CDW*, *WW*, and *obs* indicate the end-members of ice, CDW, Winter water, and in situ observations at K5. In previous studies, meltwater fraction calculation and end-member selection have used summer observation data^{20,24,25,26,27}. In this study, an end-member applicable over the entire season was required to calculate the meltwater fraction using mooring data. However, winter water is generated as a result of brine rejection and convection by sea surface cooling and remains until summer at the low layer. Thus, to detect this ‘pure’ winter water, we selected end-member estimated from summer observation already presented. We used the two-year average (2014 and 2016) end member for CDW (T ~0.013 °C, S ~34.46), WW (T ~ -1.88 °C, S ~34.24) and ice (T ~ -95 °C, S ~0) obtained from previous studies in the Amundsen Sea²⁰.

Parameterization of drag coefficient between atmosphere, sea ice, and ocean

The processes of momentum exchange between the atmosphere and ocean are complicated on the continental shelf around Antarctica because wind forcing will be delivered to the ocean through sea ice. Therefore, the atmospheric and oceanic drag coefficients are salient parameters for estimating the effect of wind forcing on the variability of seawater circulation. The drag coefficient is determined by the speed reduction and veering of sea ice. We obtained wind data from the Antarctic Mesoscale Prediction System (AMPS), which uses the Polar Weather Research and Forecasting (WRF) model, the mesoscale model specially adapted for polar regions²⁸ providing gridded wind data above 10 m at the sea surface with a horizontal resolution of 20 km (Mar. 06, 2006 to Oct. 31, 2008), 15 km (Nov. 1, 2008 to Dec. 31, 2012), and 10 km (Jan. 1, 2013 to Dec. 31, 2016) at 3 hour intervals (Supplementary Fig. 5b). Sea ice concentration data with a horizontal resolution of 3.125 km were obtained from the Advanced Microwave Scanning Radiometer for Earth observing system (AMSR-E, Jan. 1, 2006 to Oct. 4, 2011), the Special Sensor Microwave Imager/Sounder (SSMIS, Oct. 4, 2011 to Jul. 1, 2012), and the Advanced Microwave Scanning Radiometer-2 (AMSR-2, Jul. 2, 2012 to present)²⁹. Although the horizontal resolution of SSMIS is relatively low compared with the other two datasets, we interpolated the sea ice concentration to the same grid spacing as the AMSR-E. For sea ice velocity, data provided by the Polar Pathfinder Daily 25 km EASE-Grid Sea Ice Motion Vectors Version 3 from 2006 to 2016 were used³⁰.

The free drift sea ice motion using the Coriolis force, balance of wind, and water stress³¹ then becomes:

$$\rho_a C_{D,ai} |W_{10}| W_{10} + R(\theta_w) \rho_w C_{D,io} |U_w - U_{ice}| (U_w - U_{ice}) + R\left(\frac{\pi}{2}\right) \rho_{ice} h f (U_w - U_{ice}) = 0 \quad (6)$$

where $C_{D,ai}$ is drag coefficient between the air and ice; W_{10} is surface wind; U_w , and U_{ice} are the ocean current and sea ice velocities, respectively; ρ_a , ρ_w , and ρ_{ice} are the densities of air, water, and sea ice, respectively; f is the Coriolis parameter; and h is ice thickness. The rotation matrix R as a function of the angle (θ) between $(U_{ice} - U_w)$ and W_{10} is given by:

$$R(\theta) = \begin{pmatrix} \cos\theta & -\sin\theta \\ \sin\theta & \cos\theta \end{pmatrix} \quad (7)$$

The U_{ice} as sea ice velocity can be expressed as:

$$U_{ice} = \alpha R(-\theta)W_{10} + U_w \quad (8)$$

where α is the wind factor. If U_{ice} is assumed to be far larger than U_w , the ice-ocean drag coefficient ($C_{D,io}$) can be estimated, allowing sea ice motion and sea ice velocity in free drift to be defined as³²:

$$\alpha^4 + N_a^2 R_o^2 \alpha^2 - N_a^4 = 0 \quad (9)$$

where N_a is the Nansen Number and R_o is the ice's Rossby Number, given by:

$$N_a = \sqrt{\frac{\rho_a C_{D,ai}}{\rho_w C_{D,io}}} \text{ and } R_o = \frac{\rho_{ice} H f}{\rho_w C_{D,io} N_a |W_{10}|} \quad (10)$$

The wind factor (α) and angle (θ) can be written as:

$$\alpha = N_a \sqrt{\frac{\sqrt{R_o^4 + 4} - R_o^2}{2}} \quad (11)$$

$$\theta = \arctan\left(\frac{N_a R_o}{\alpha}\right) = \arctan\left(\frac{1}{\sqrt{\frac{1}{4} + \frac{1}{R_o^4} - \frac{1}{2}}}\right) \quad (12)$$

The observation data can be calculated from each grid point as³³:

$$\alpha = \frac{\cos(\theta) \sum W_{10}^{x'} U_{ice}^{x'} + \sin(\theta) \sum W_{10}^{y'} U_{ice}^{y'} - \sin(\theta) \sum W_{10}^{x'} U_{ice}^{y'} + \cos(\theta) \sum W_{10}^{y'} U_{ice}^{x'}}{\sum U_{ice}^{x'}{}^2 - \sum U_{ice}^{y'}{}^2} \quad (13)$$

$$\theta = \arctan \left(\frac{\sum W_{10}^{x'} U_{ice}^{y'} - \sum W_{10}^{y'} U_{ice}^{x'}}{\sum W_{10}^{x'} U_{ice}^{x'} - \sum W_{10}^{y'} U_{ice}^{y'}} \right) \quad (14)$$

Finally, using the functions above for θ and α , the expressions for N_a and R_o become:

$$N_a = \frac{\alpha}{\sqrt{\frac{\frac{1}{\left(\frac{1}{\tan^2 \theta + 2}\right)^2 - \frac{1}{4}} + 4 - \frac{1}{\left(\frac{1}{\tan^2 \theta + 2}\right)^2 - \frac{1}{4}}}{2}}} \quad (15)$$

$$R_o = \frac{1}{\sqrt[4]{\left(\frac{1}{\tan^2 \theta + 2}\right)^2 - \frac{1}{4}}} \quad (16)$$

where $W_{10}^{x'}$, $W_{10}^{y'}$, $U_{ice}^{x'}$, and $U_{ice}^{y'}$ are anomalies defined by $(W_{10}^x - \dot{W}_{10}^x)$, $(W_{10}^y - \dot{W}_{10}^y)$, $(U_{10}^x - \dot{U}_{10}^x)$, and $(U_{ice}^y - \dot{U}_{ice}^y)$, and U_{ice}^x , U_{ice}^y , \dot{W}_{10}^x , and \dot{W}_{10}^y , are sea ice velocities of zonal and meridional direction and mean values of 10 m wind, respectively. Finally, the $C_{D,io}$ and $C_{D,ai}$ can be calculated from N_a , R_o and the mean sea ice thickness (<https://neptune.gsfc.nasa.gov/csb/index.php?section=272>)

^{34,35} in spring and autumn from 2004 to 2007 as obtained from NASA's Ice, Cloud, and land Elevation Satellite (ICESat) laser altimetry (Supplementary Fig. 5):

$$C_{D,io} = \frac{\rho_{ice} H f}{\rho_w R_o N_a |W_{10}|} \text{ and } C_{D,ai} = \frac{\rho_w C_{D,io} N_a^2}{\rho_a} \quad (17)$$

Ocean surface stress curl calculations

In the coastal region, the horizontal imbalance of energy from the atmosphere into the ocean can have a large impact on ocean circulation. Therefore, ocean circulation will be strengthened by horizontal variations in the wind field and sea ice condition at the boundary of the polynya. Ocean surface stress is calculated as a combination of sea ice and wind stress as:

$$\tau_o = A \tau_{io} + (1 - A) \tau_{ao} \quad (18)$$

where A is the portion of the area occupied by sea ice and τ_{ao}, τ_{io} are the ocean surface stress at the air-ocean and ice-ocean interface, respectively^{36,37}. τ_{ao} was calculated by:

$$\tau_{ao} = (\tau_{ao}^x, \tau_{ao}^y) = \rho_a C_{D,ao} |W_{10}| W_{10} \quad (19)$$

where subscript x and y are the zonal and meridional components, respectively; ρ_a and W_{10} are the air density (1.29 kg m^{-3}) and wind velocity vector at 10 m above the sea level, respectively. The air-ocean drag coefficient ($C_{D,ao}$) was applied depending on wind speed as³⁸:

$$C_{D,ao} = \begin{cases} 1.2 \times 10^{-3} & W_{10} < 11 \text{ ms}^{-1} \\ (0.49 + 0.065 W_{10}) \times 10^{-3} & 11 \leq W_{10} \leq 25 \text{ ms}^{-1} \end{cases} \quad (20)$$

ice-ocean surface stress (τ_{io}) was calculated as follows:

$$\tau_{io} = (\tau_{io}^x, \tau_{io}^y) = \rho_w C_{D,io} |U_{ice} - U_w| (U_{ice} - U_w) \quad (21)$$

where ρ_w is the surface water density (1026 kg m^{-3}); U_{ice} is the sea ice velocity (observation)³⁰; and U_w is the water velocity^{37,39}. Understandably, the water velocity was unknown below ice coverage in the Amundsen Sea. Thus, we estimated a parameterization assuming that a full Ekman spiral developed below the ice and that no other forces than the stress were acting on the water; this gave the surface current velocities as^{37,40,41}:

$$\begin{pmatrix} U_w^x \\ U_w^y \end{pmatrix} = \begin{pmatrix} \cos\left(\frac{\pi}{4}\right) & -\sin\left(\frac{\pi}{4}\right) \\ \sin\left(\frac{\pi}{4}\right) & \cos\left(\frac{\pi}{4}\right) \end{pmatrix} \begin{pmatrix} \frac{\tau_o^x}{\sqrt{\rho_w^2 f A_z}} \\ \frac{\tau_o^y}{\sqrt{\rho_w^2 f A_z}} \end{pmatrix} \quad (22)$$

where f is the Coriolis parameter, A_z is the vertical eddy viscosity of 0.1, and τ_o^x, τ_o^y are the surface stresses. The surface current velocity was calculated by repeating the above equations, starting at the surface with a current velocity of zero and continuing until convergence. Finally, ocean surface stress curl (τ_c) was written as :

$$\tau_c = -\left(\frac{\partial \tau_x}{\partial y} - \frac{\partial \tau_y}{\partial x}\right) \quad (23)$$

References

1. Pritchard, H. D. et al. Antarctic ice-sheet loss driven by basal melting of ice shelves. *Nature* **484**, 502–505 (2012).
2. Rignot, E., Jacobs, S., Mouginot, J. & Scheuchl, B. Ice-shelf melting around Antarctica. *Science* **341**, 266–270 (2013).
3. Depoorter, M. A. et al. Calving fluxes and basal melt rates of Antarctic ice shelves. *Nature* **502**, 89–92 (2013).
4. Harig, C. & Simons, F. J. Accelerated West Antarctic ice mass loss continues to outpace East Antarctic gains. *Earth Planet. Sci. Lett.* **415**, 134–141 (2015).
5. Paolo, F. S., Fricker, H. A. & Padman, L. Volume loss from Antarctic ice shelves is accelerating. *Science* **348**, 327–331 (2015).
6. Thomas, R. H., Rignot, E., Kanagaratnam, P., Krabill, W. & Casassa, G. Force-perturbation analysis of Pine Island Glacier, Antarctica, suggests cause for recent acceleration. *Ann. Glaciol.* **39**, 133–138 (2004).
7. Shepherd, A. et al. A reconciled estimate of ice-sheet mass balance. *Science* **338**, 1183–1189 (2012).
8. Scambos, T. A. et al. How much, how fast? : A science review and outlook for research on the instability of Antarctica's Thwaites Glacier in the 21st century. *Global and Planetary Change.* **153**, 16–34 (2017).
9. Walker, D. P. et al. Oceanic heat transport onto the Amundsen Sea shelf through a submarine glacial trough. *Geophys. Res. Lett.* **34**, L02602 (2007).
10. Jenkins, A. et al. Observations beneath Pine Island Glacier in West Antarctica and implications for its retreat. *Nature Geosci.* **3**, 468–472 (2010).
11. Wåhlin, A. K., Yuan, X., Björk, G. & Nohr, C. Inflow of warm circumpolar deep water in the central Amundsen shelf. *J. Phys. Oceanogr.* **40**, 1427–1434 (2010).
12. Wåhlin, A. K. et al. Some implications of Ekman layer dynamics for cross-shelf exchange in the Amundsen Sea. *J. Phys. Oceanogr.* **42**, 1461–1474 (2012).
13. Jacobs, S. S. et al. The Amundsen Sea and the Antarctic Ice Sheet. *Oceanogr.* **25**, 154–163 (2012).
14. Arneborg, L., Wåhlin, A. K., Björk, G., Liljebladh, B. & Orsi, A. H. Persistent inflow of warm water onto the central Amundsen shelf. *Nature Geosci.* **5**, 876–880 (2012).
15. Dutrieux, P. et al. Strong sensitivity of Pine Island ice-shelf melting to climatic variability. *Science* **343**, 174–178 (2014).

16. Wåhlin, A. K. et al. Variability of warm deep water inflow in a submarine trough on the Amundsen Sea shelf. *J. Phys. Oceanogr.* **43**, 2054–2070 (2013).
17. Kim, T. W. et al. Is Ekman pumping responsible for the seasonal variation of warm circumpolar deep water in the Amundsen Sea? *Cont. Shelf Res.* **132**, 38–48 (2017).
18. Jacobs, S. S., Jenkins, A., Giulivi, C. F. & Dutriex, P. Stronger ocean circulation and increased melting under Pine Island Glacier ice shelf. *Nat. Geosci.* **4**, 519–523 (2011).
19. Webber, B. G. M. et al. Mechanisms driving variability in the ocean forcing of Pine Island Glacier. *Nat. Commun.* **7**, 14507 (2017).
20. Jenkins, A. et al. West Antarctic Ice Sheet retreat in the Amundsen Sea driven by decadal oceanic variability. *Nat. Geosci.* **11**, 733–738 (2018).
21. Kim, C. S. et al. Variability of the Antarctic coastal current in the Amundsen Sea. *Estuar. Coast. Shelf Sci.* **181**, 123–133 (2016).
22. Wåhlin, A. et al. Ice front of ocean heat transport to an Antarctic ice shelf. *Nature* **578**, 568–571 (2020).
23. Pawlowicz, R., Beardsley, B. & Lentz, S. Classical tidal harmonic analysis including error estimates in MATLAB using T_TIDE. *Comput. Geosci.* **28**, 929–937 (2002).
24. Randall-Goodwin, E., et al. Freshwater distributions and water mass structure in the Amundsen Sea Polynya region, Antarctica. *Elem. Sci. Anth.* **3**, (2015)
25. Jenkins, A. The impact of melting ice on ocean waters. *J. Phys. Oceanogr.* **29**, 2370–2381 (1999).
26. Jenkins, A. & Jacobs, S. S. Circulation and melting beneath George VI Ice Shelf, Antarctica. *J. Geophys. Res.* **113**, C04013 (2008).
27. Miles, T. et al. Glider observations of the Dotson Ice Shelf outflow. *Deep Sea Res. Part II: Top. Stud. Oceanography* **123**, 16–29 (2016).
28. Bumbaco, K. A. et al. Evaluating the Antarctic Observational Network with the Antarctic Mesoscale Prediction System (AMPS). *Mon. Weather Rev.* **142**, 3847–3859 (2014).
29. Spreen, G., Kaleschke, L. & Heygster, G. Sea ice remote sensing using AMSR-E 89-GHz channels. *J. Geophys. Res.* **113**, C02S03 (2008)
30. Tschudi, M., Fowler, C., Maslanik, J., Stewart, J. S. & Meier, W. *Polar Pathfinder Daily 25 km EASE-Grid Sea Ice Motion Vectors* Version 3 (National Snow and Ice Data Center, 2016).
31. Leppäranta, M. *The Drift of Sea Ice* (Springer, Berlin, 2005).
32. Lu, P., Li, Z. & Han, H. Introduction of parameterized sea ice drag coefficients into ice free-drift modeling. *Acta Oceanol. Sin.* **35**, 53–59 (2016).

33. Kimura, N. Sea ice motion in response to surface wind and ocean current in the Southern Ocean. *J. Meteorolog. Soc. Japan. Ser. II* **82**, 1223–1231 (2004).
34. Kurtz, N.T. & T. Markus. Satellite observations of Antarctic sea ice thickness and volume. *J. Geophys. Res.* **117**, C08025 (2012).
35. Markus, T. et al. Freeboard, snow depth, and sea ice roughness in East Antarctica from in-situ and multiple satellite data. *Ann. Glaciol.* **52**, 242–248 (2011).
36. Yang, J. The seasonal variability of the Arctic Ocean Ekman transport and its role in the mixed layer heat and salt fluxes. *J. Clim.* **19**, 5366–5387 (2006).
37. Timmermann, R. et al. Ocean circulation and sea ice distribution in a finite element global sea ice–ocean model. *Ocean Model.* **27**, 114–129 (2009).
38. Large, W. G. & Pond, S. Open ocean momentum flux measurements in moderate to strong winds. *J. Phys. Oceanogr.* **11**, 324–336 (1981).
39. Häkkinen, S. Coupled ice-ocean dynamics in the marginal ice zones: upwelling/ downwelling and eddy generation. *J. Geophys. Res. Oceans* **91**, 819–832 (1986).
40. Ekman, V. W. On the influence of the earth's rotation on ocean currents. *Ark. Mat. Astron. Fys.*, **2**, 1–53 (1905).
41. Pond, S. & Pickard, G.L. *Introductory Dynamical Oceanography* (Gulf Professional Publishing, Houston, TX, 1983).

Acknowledgement

The authors thank the officers, crew and scientists of the R/V Araon. The research was supported by the Korea Polar Research Institute (KOPRI) (PE21110). We thank three anonymous reviewers for comments that helped to improve the manuscript.

Author contributions

HY led the analysis and wrote the manuscript. TK designed the research and contributed to the data analysis. PD, AW, AJ, HH, CK, KC and SL were responsible for data collection and initial data processing. All authors contributed to writing the manuscript.

Competing interests.

The authors declare no competing financial interests.

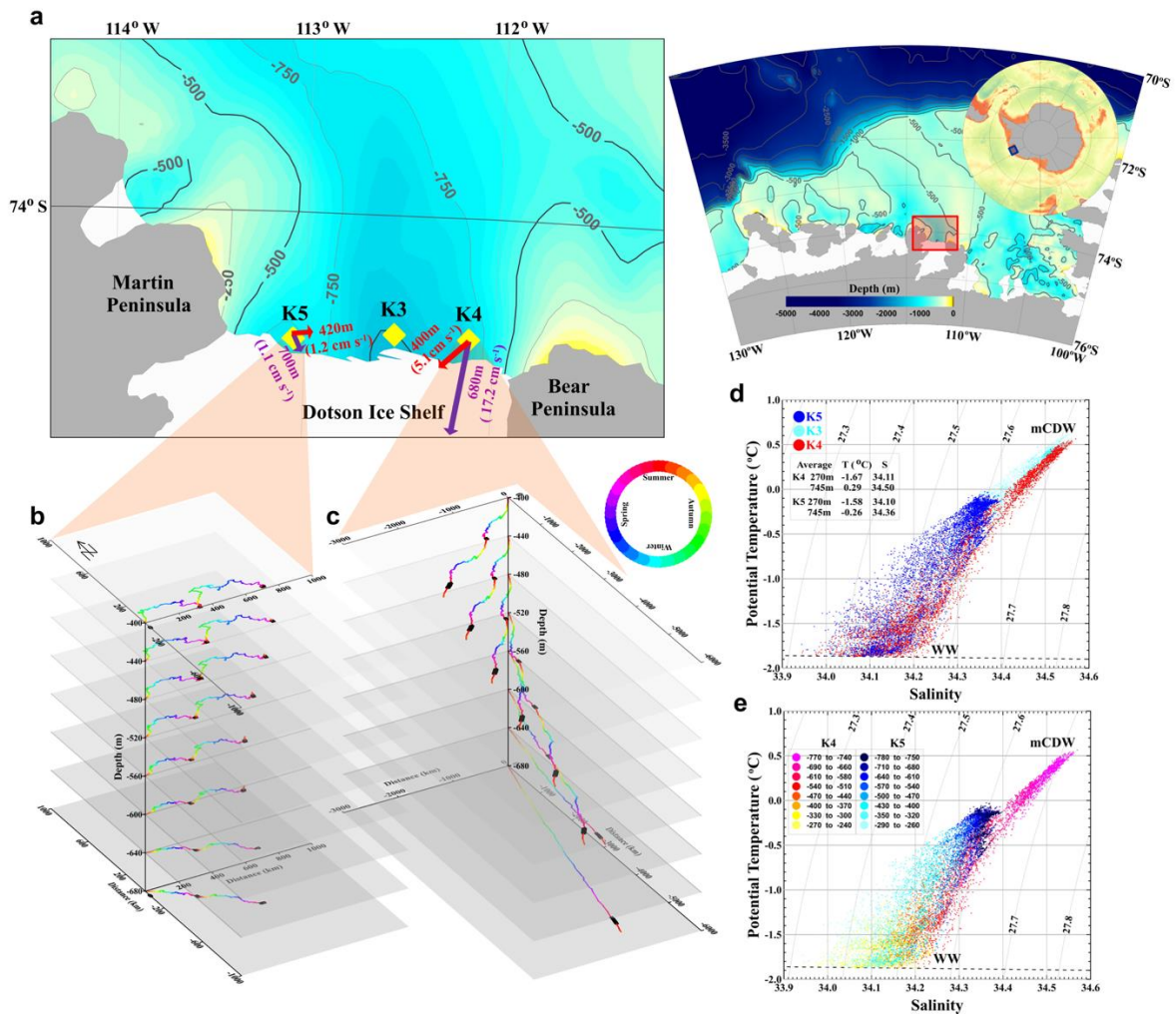


Figure 1 | Study area, bathymetry, station locations, progressive vector and temperature-salinity diagrams at mooring sites. (a) Bathymetry and stations on the Amundsen Sea continental shelf (location shown in red rectangle). Yellow diamonds show moorings K3, K4, and K5 near the Dotson Ice Shelf. Red and purple arrows are average current at the top layer (K4 = 400m, K5 = 420m) and the bottom layer (K4 = 680m, K5 = 700m). **(b & c)** Progressive vector diagrams of velocities at K5 from 420–700 m depth and K4 from 400–680 m depth during 2014 & 2015. Color-coded dots denote season; black squares indicate January 1. **(d)** Temperature-salinity at K4 (red), K3 (cyan), and K5 (blue). Average potential temperature and salinity near the top (270m) and bottom layer (745m). **(e)** Temperature-salinity color-coded by depth at K4 and K5.

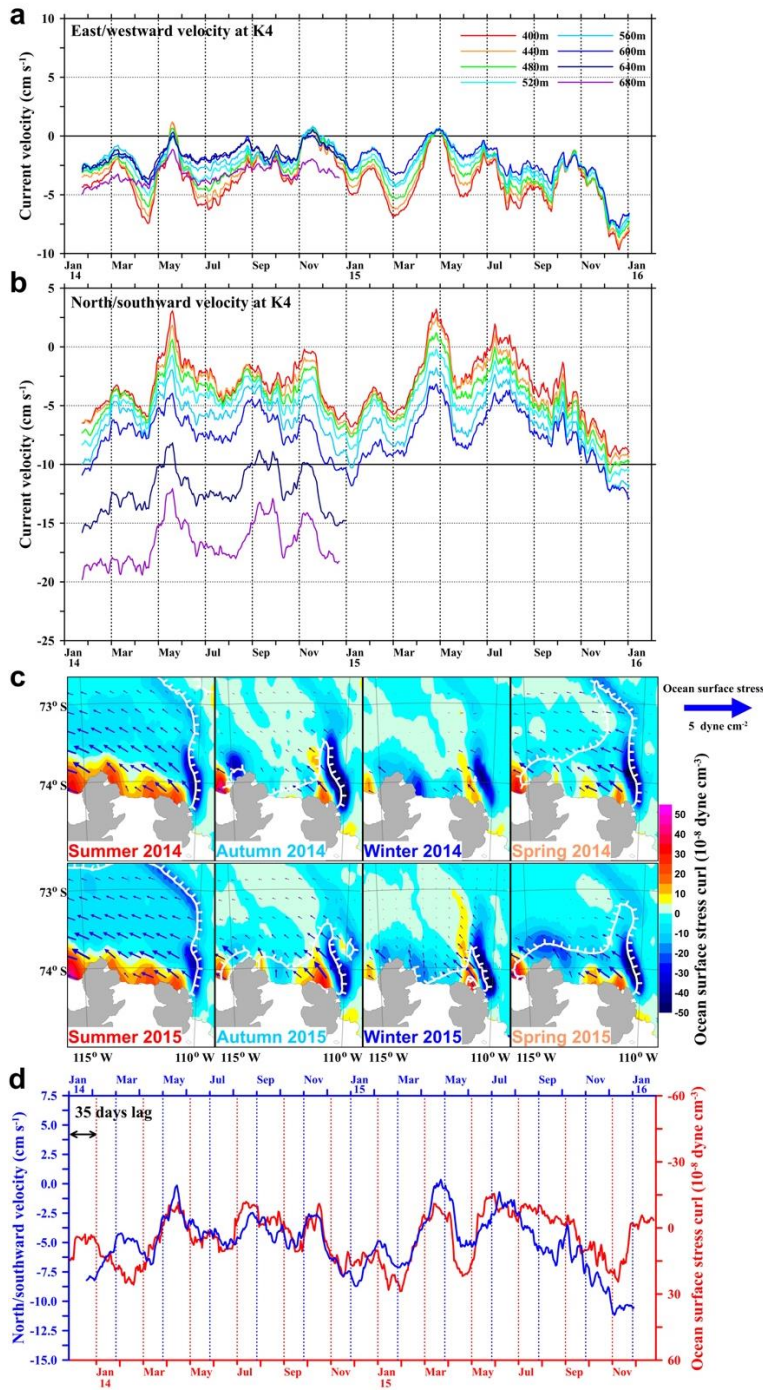


Figure 2 | Time series of velocities and ocean surface stress curl. (a & b) 31 day running average zonal and meridional velocities at K4. Positive value is east and northward current. (c) horizontal distribution of ocean surface stress curl (color), ocean surface stress (arrow) and sea ice concentration (SIC) in 2014 and 2015. Uphill side of white hatched line indicates where SIC is over 50%. A positive OSSC means high sea surface height. (d) 31day running average OSSC at 74°S, 112.25°W (red) and vertical mean (400–600 m) meridional velocity (blue). Lower x-axis is back-shifted by 35 days.

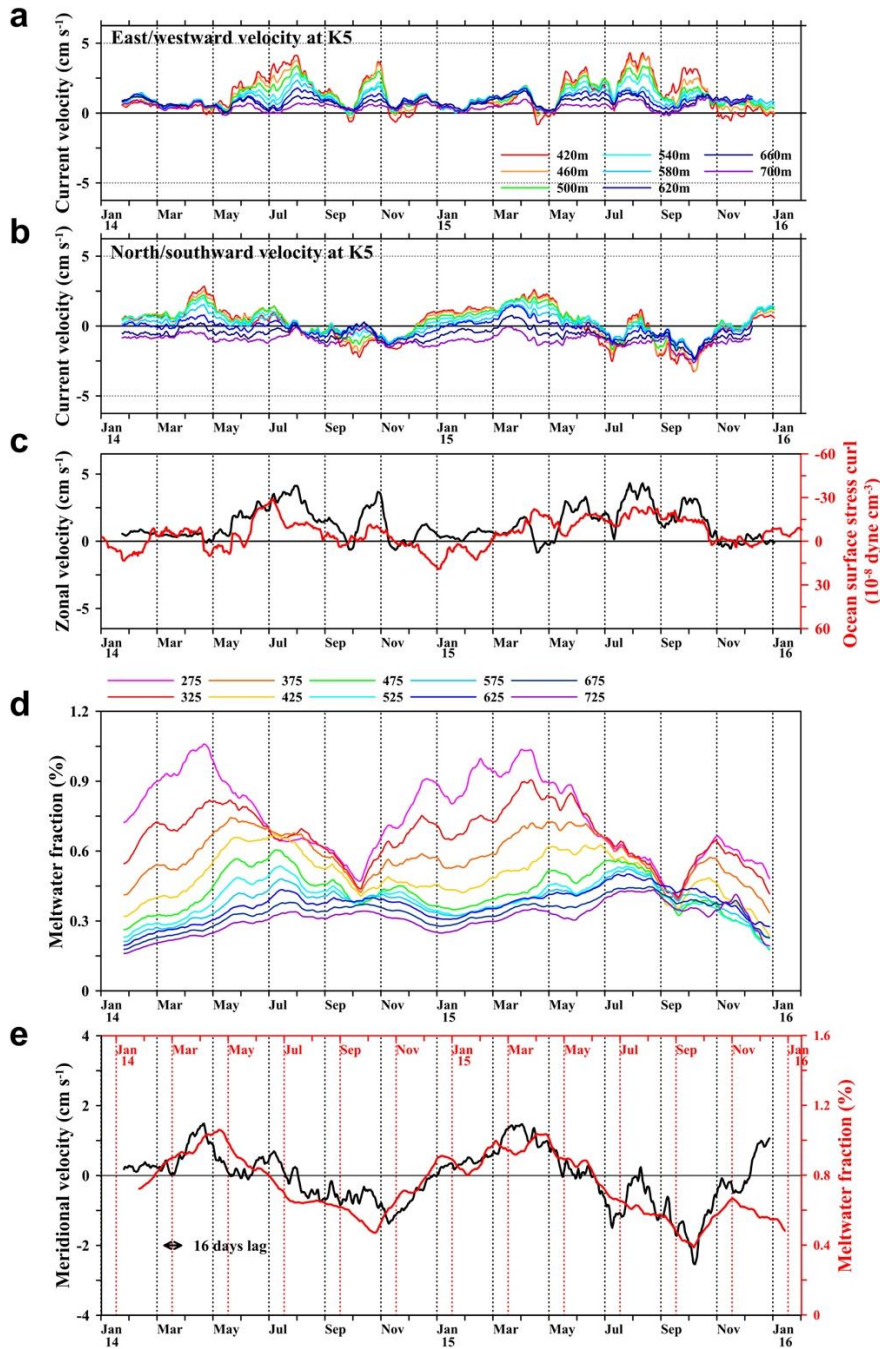


Figure 3 | Time series of velocities and meltwater fraction at K5. (a & b) 31 day running average zonal and meridional velocities at K5. **(c)** 31 day running average zonal velocity (420m, black line) and mean OSSC (74°S, 112.75 - 113.25°W, red line). It showed a good correlation as $r = 0.57$. **(d)** 31 day running average meltwater fraction at 50 m intervals from 275–725 m (thin color-coded lines). **(e)** 31 day running average velocity (vertical mean, black line) and meltwater fraction (red line) at 275 m.

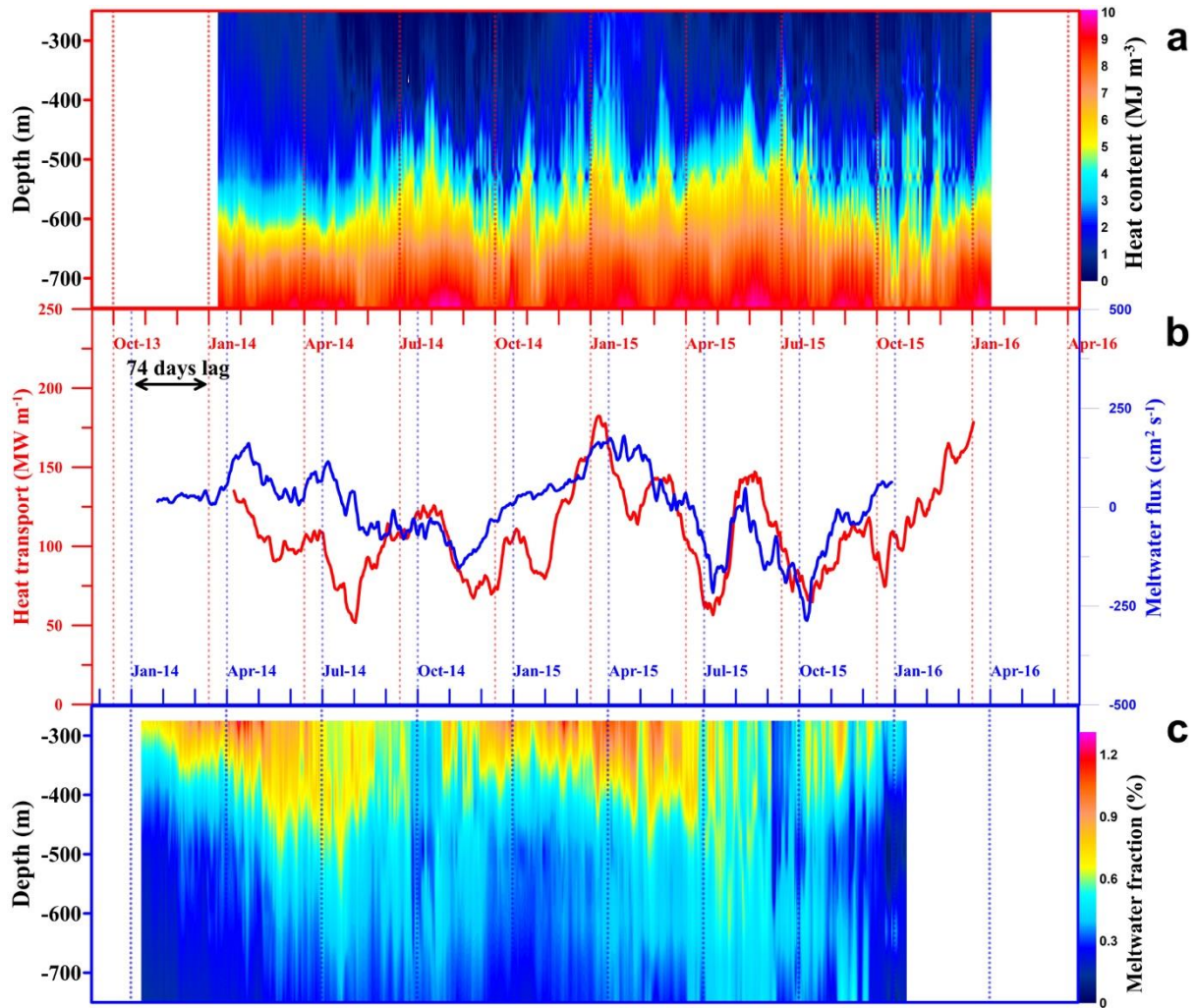


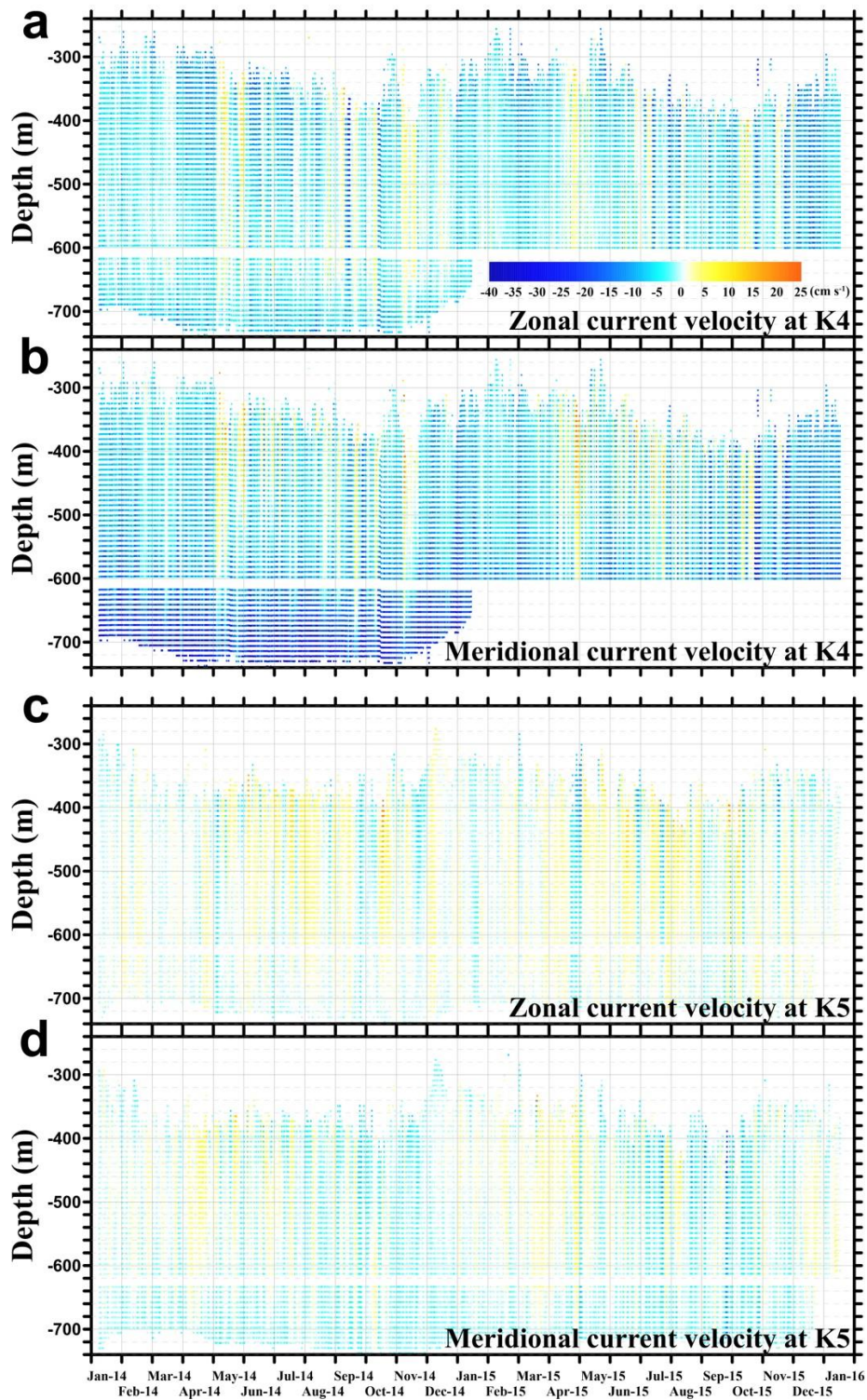
Figure 4 | Time series of heat content and heat transport at K4 and meltwater fraction and meltwater flux at K5. (a) Vertical and temporal distribution of calculated heat content from 250–750 m at K4. **(b)** 31 day running average vertical mean meltwater flux (blue) between 275–575 m at mooring K5 and estimated heat transport (red) at mooring K4. The upper x-axis for heat transport and content has been back-shifted 74 days. **(c)** Vertical and temporal distribution of meltwater fraction at mooring K5.

Supplementary Materials

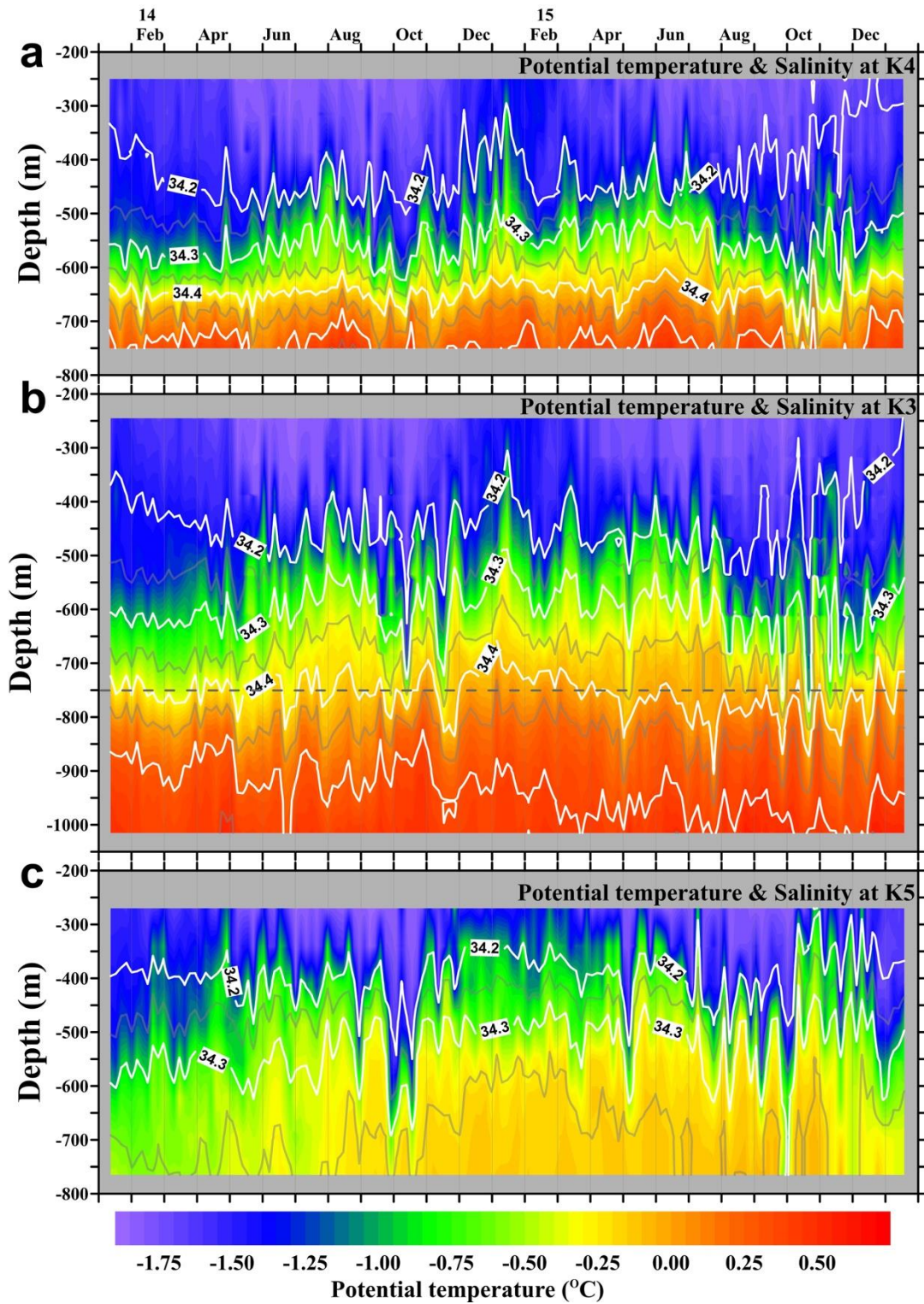
Supplementary Table 1 Mooring details

| Station | Depth | Latitude Longitude | Observation Period (MM/DD/YYYY) | Instruments | Reference |
|---------|--------|---------------------------------|------------------------------------|---------------|---------------------------|
| K4 | 785 m | 74° 10.576' S 112° 8.083' W | 01/08/2014 – 01/19/2016 | 150 kHz ADCP | Upward-looking at 610 m |
| | | | 01/08/2014 – 01/14/2015 | 300 kHz ADCP | Downward-looking at 612 m |
| | | | 01/08/2014 – 12/22/2015 | SBE37-SMP-ODO | 249 m |
| | | | 01/08/2014 – 01/19/2016 | SBE37-SM | 314 m |
| | | | 01/08/2014 – 01/19/2016 | SBE37-SM | 385 m |
| | | | 01/08/2014 – 01/19/2016 | SBE37-SM | 457 m |
| | | | 01/08/2014 – 01/19/2016 | SBE37-SMP-ODO | 527 m |
| | | | 01/08/2014 – 01/19/2016 | SBE37-SM | 598 m |
| | | | 01/08/2014 – 01/19/2016 | SBE37-SM | 675 m |
| | | | 01/08/2014 – 01/19/2016 | SBE37-SM | 747 m |
| K3 | 1028 m | 74° 10.292' S 112° 31.699' W | 01/09/2014 – 01/11/2015 | 75 kHz ADCP | Upward-looking at 905 m |
| | | | 01/09/2014 – 01/02/2016 | 300 kHz ADCP | Downward-looking at 907 m |
| | | | 01/09/2014 – 01/19/2016 | SBE37-SM | 247 m |
| | | | 01/09/2014 – 01/19/2016 | SBE37-SM | 317 m |
| | | | 01/09/2014 – 01/19/2016 | SBE37-SM | 388 m |
| | | | 01/09/2014 – 01/19/2016 | SBE37-SM | 468 m |
| | | | 01/09/2014 – 01/19/2016 | SBE37-SM | 539 m |
| | | | 01/09/2014 – 01/19/2016 | SBE37-SM | 610 m |
| | | | 01/09/2014 – 01/19/2016 | SBE37-SM | 682 m |
| | | | 01/09/2014 – 01/19/2016 | SBE37-SM | 752 m |
| | | | 01/09/2014 – 01/19/2016 | SBE37-SM | 823 m |
| | | | 01/09/2014 – 01/19/2016 | SBE37-SM | 894 m |
| | | | 01/09/2014 – 01/19/2016 | SBE37-SM | 955 m |
| | | | 01/09/2014 – 01/19/2016 | SBE37-SM | 1015 m |
| K5 | 774 m | 74° 10.946' S 113° 3.823' W | 01/09/2014 – 01/20/2016 | 150 kHz ADCP | Upward-looking at 625 m |
| | | | 01/09/2014 – 12/24/2015 | 300 kHz ADCP | Downward-looking at 627 m |
| | | | 01/09/2014 – 01/20/2016 | SBE37-SMP-ODO | 272 m |
| | | | 01/09/2014 – 01/20/2016 | SBE37-SM | 342 m |
| | | | 01/09/2014 – 01/20/2016 | SBE37-SM | 412 m |
| | | | 01/09/2014 – 01/20/2016 | SBE37-SMP-ODO | 483 m |
| | | | 01/09/2014 – 01/20/2016 | SBE37-SM | 553 m |
| | | | 01/09/2014 – 01/20/2016 | SBE37-SM | 622 m |
| | | | 01/09/2014 – 01/20/2016 | SBE37-SM | 695 m |
| | | | 01/09/2014 – 01/20/2016 | SBE37-SM | 768 m |

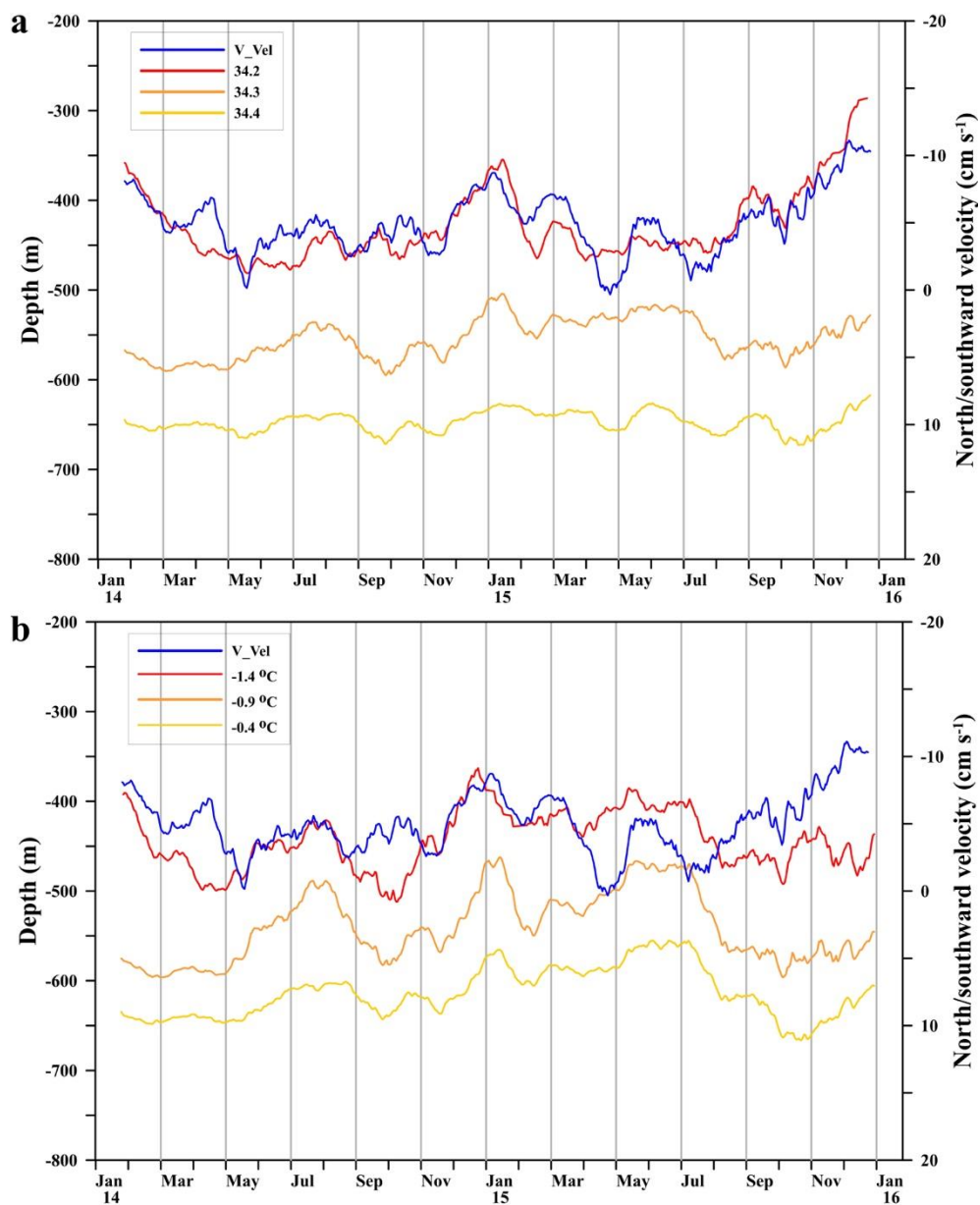
High resolution mooring systems deployed on January 8–9, 2014 and recovered on January 19–20, 2016 at three locations: K3 (trough center), K4 (east), and K5 (west) to measure the temporal variability and properties of mCDW near the Dotson Ice Shelf. All moorings used dual-ADCP (Acoustic Doppler Current Profilers) consisting of upward-looking 150 kHz (K4 and K5) or 75 kHz (K3) and downward-looking 300 kHz units, along with 8 (K4 and K5) or 12 (K3) Sea-Bird Electronic (SBE) 37-SM or 37-SMP-ODO MicroCATs.



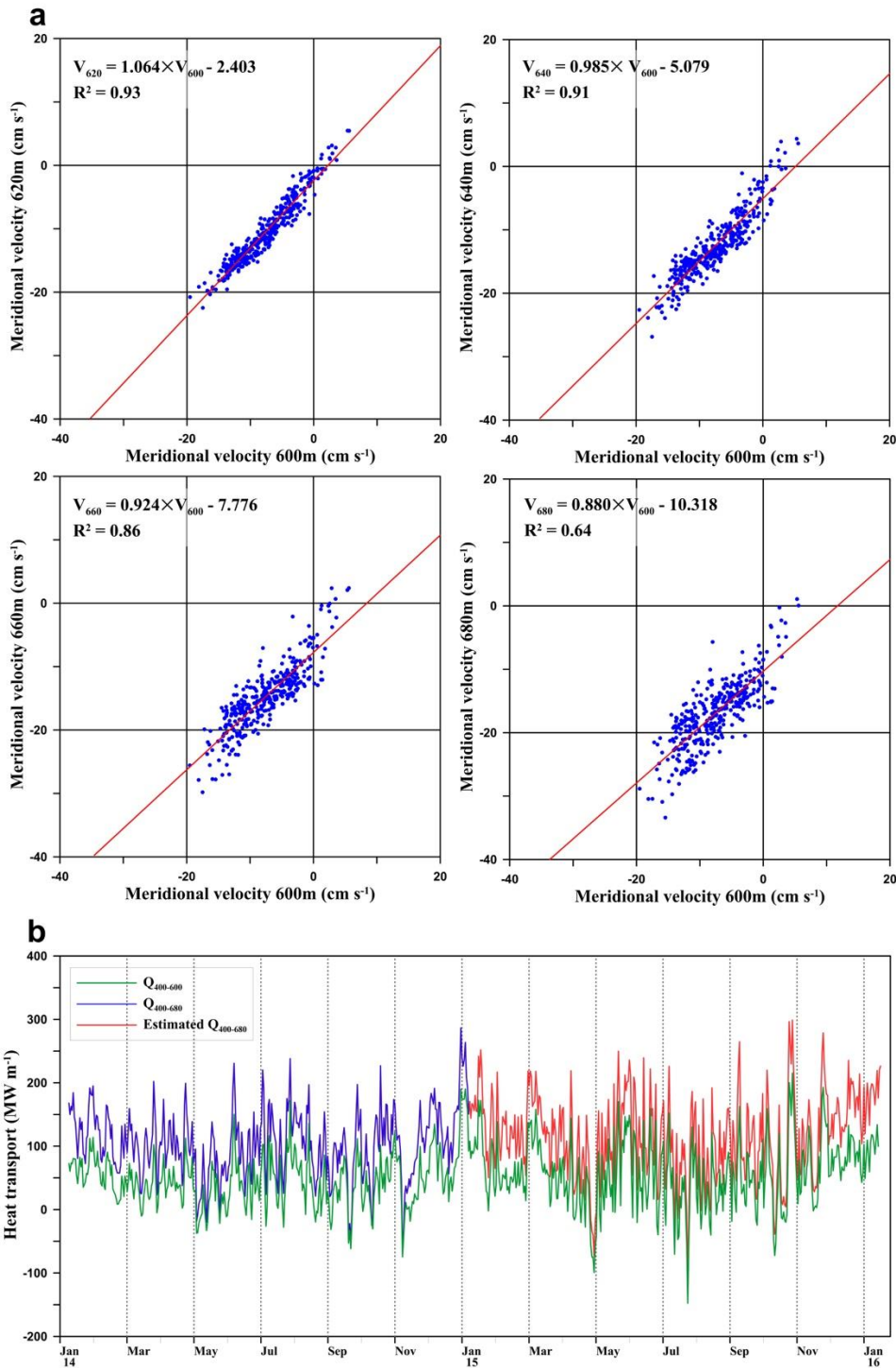
Supplementary Figure 1 | Daily average current velocities at K4 and K5, measured with dual-ADCP (Acoustic Doppler Current Profiler) systems with upward-looking 150 kHz and downward-looking 300 kHz units. (a & b) Zonal and meridional current velocities at mooring K4. (c & d) Zonal and meridional current velocities at mooring K5.



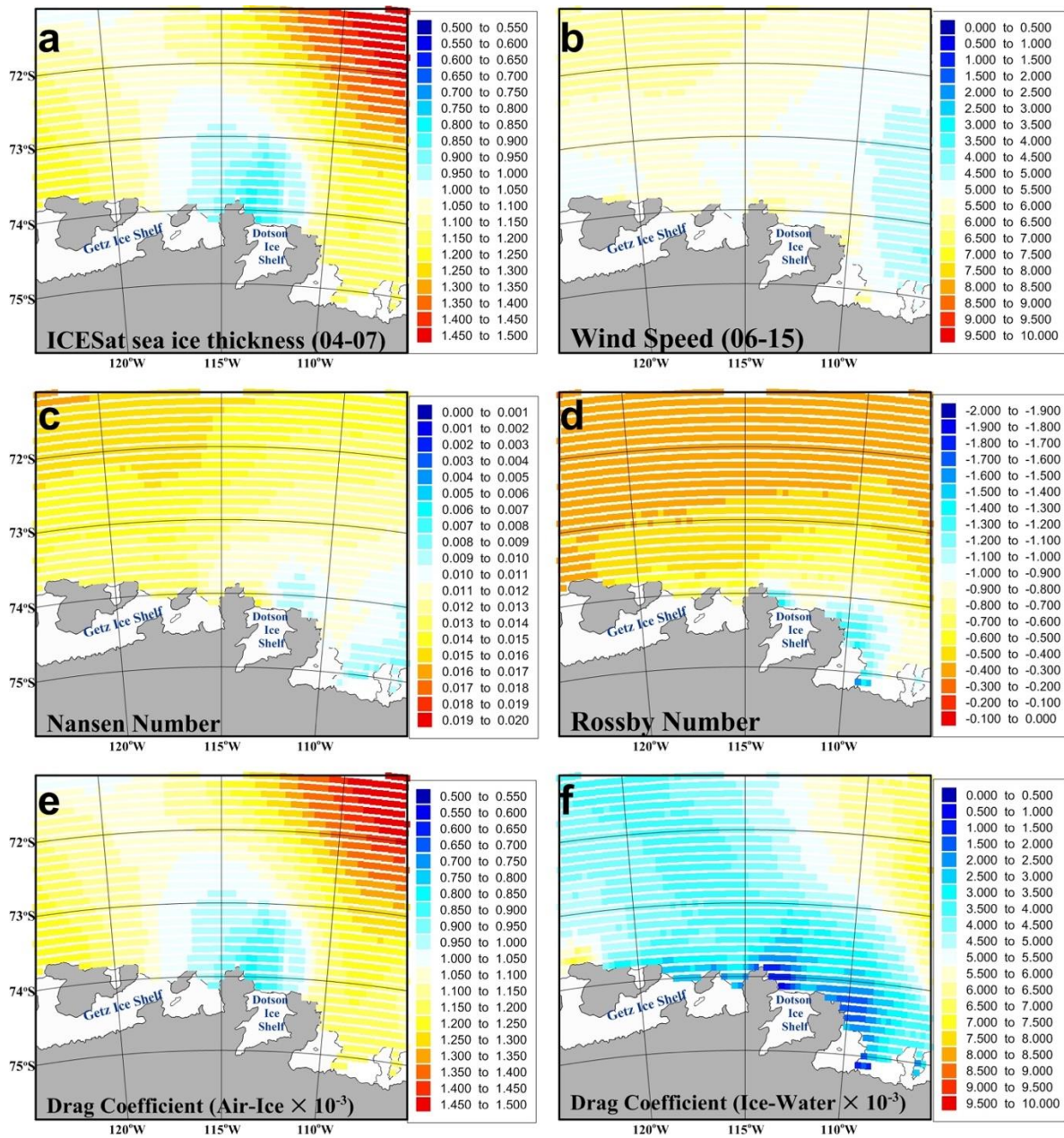
Supplementary Figure 2 | Time series of vertical temperature and salinity at (a) K4, (b) K3, and (c) K5. Temperature (color) and salinity (white line) were measured by Sea-Bird 37-SM or 37-SMP-ODO MicroCATs from early January 2014 to mid-January 2016.



Supplementary Figure 3 | Seasonal variation of salinity, potential temperature and velocity at K4. (a) 31 day moving average variation of salinity (red, orange, and yellow lines) and meridional velocity (blue line). (b) 31 day moving average variation of potential temperature and meridional velocity. Salinity (34.2, red) and potential temperature (-1.4°C, red) show a good correlation with meridional velocity.



Supplementary Figure 4 | Estimating meridional velocity below 600 m at K4. (a) Regression of velocities between 600 m and 620 m, 640 m, 660 m, and 680 m. **(b)** Time series of heat transport from 400–600 m over two years (green) and from 400–680 m over one year (blue). Heat transport from 400–680 m was extended over two years (red) using the estimated velocity from (a).



Supplementary Figure 5 | Horizontal distribution of six parameters. (a) Average sea ice thickness during spring and autumn 2004–2007, from ICESat^{35,36}. (b) Average daily wind speed, 2006–2015, from the Antarctic Mesoscale Prediction System²⁸. (c–f) Horizontal distributions of calculated Nansen and Rossby numbers, along with air-ice and ice-ocean drag coefficients.

Figures

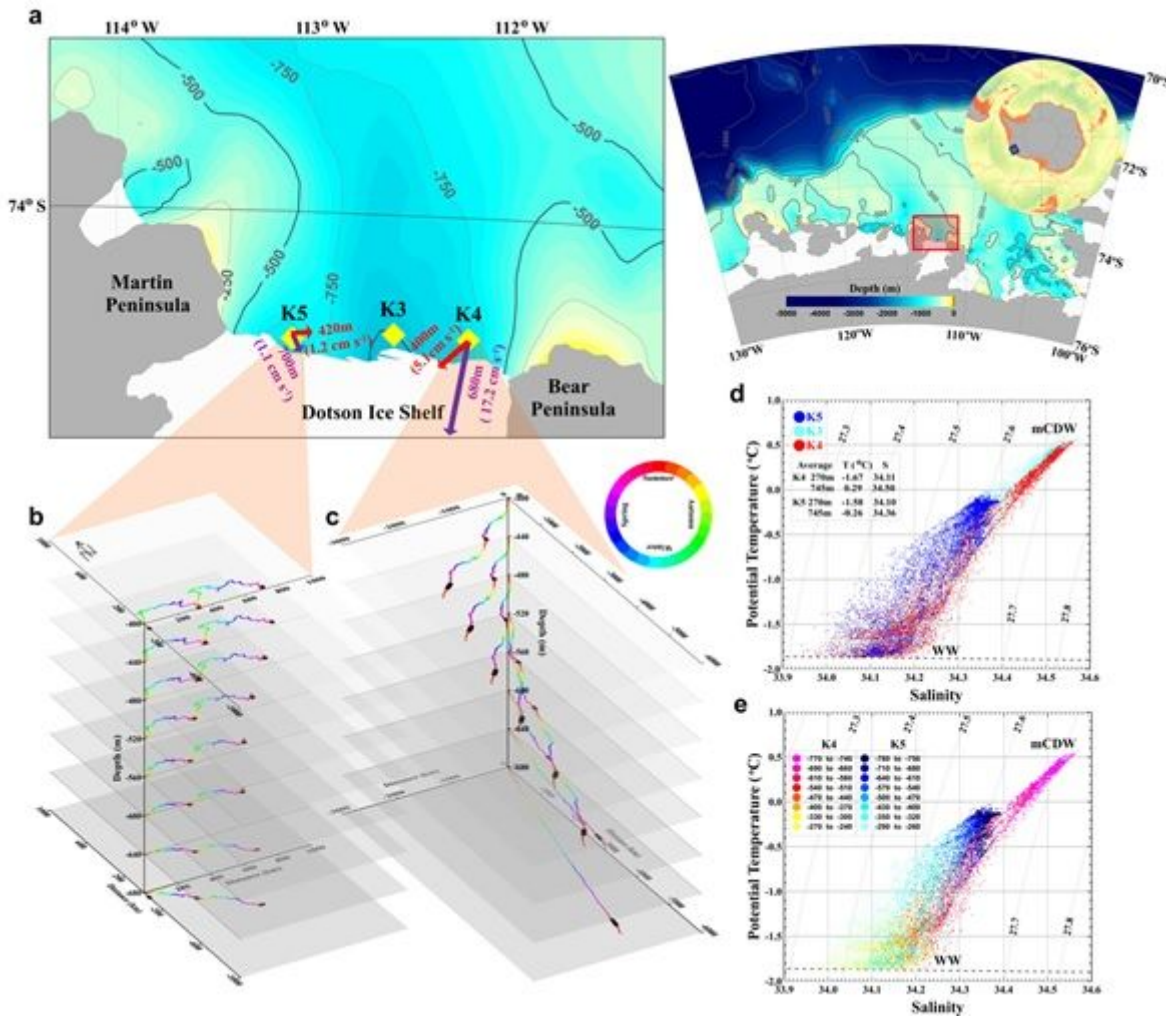


Figure 1

Study area, bathymetry, station locations, progressive vector and temperature-salinity diagrams at mooring sites. (a) Bathymetry and stations on the Amundsen Sea continental shelf (location shown in red rectangle). Yellow diamonds show moorings K3, K4, and K5 near the Dotson Ice Shelf. Red and purple arrows are average current at the top layer (K4 = 400m, K5 = 420m) and the bottom layer (K4 = 680m, K5 = 700m). (b & c) Progressive vector diagrams of velocities at K5 from 420–700 m depth and K4 from 400–680 m depth during 2014 & 2015. Color-coded dots denote season; black squares indicate January 1. (d) Temperature-salinity at K4 (red), K3 (cyan), and K5 (blue). Average potential temperature and salinity near the top (270m) and bottom layer (745m). (e) Temperature-salinity color-coded by depth at K4 and K5.

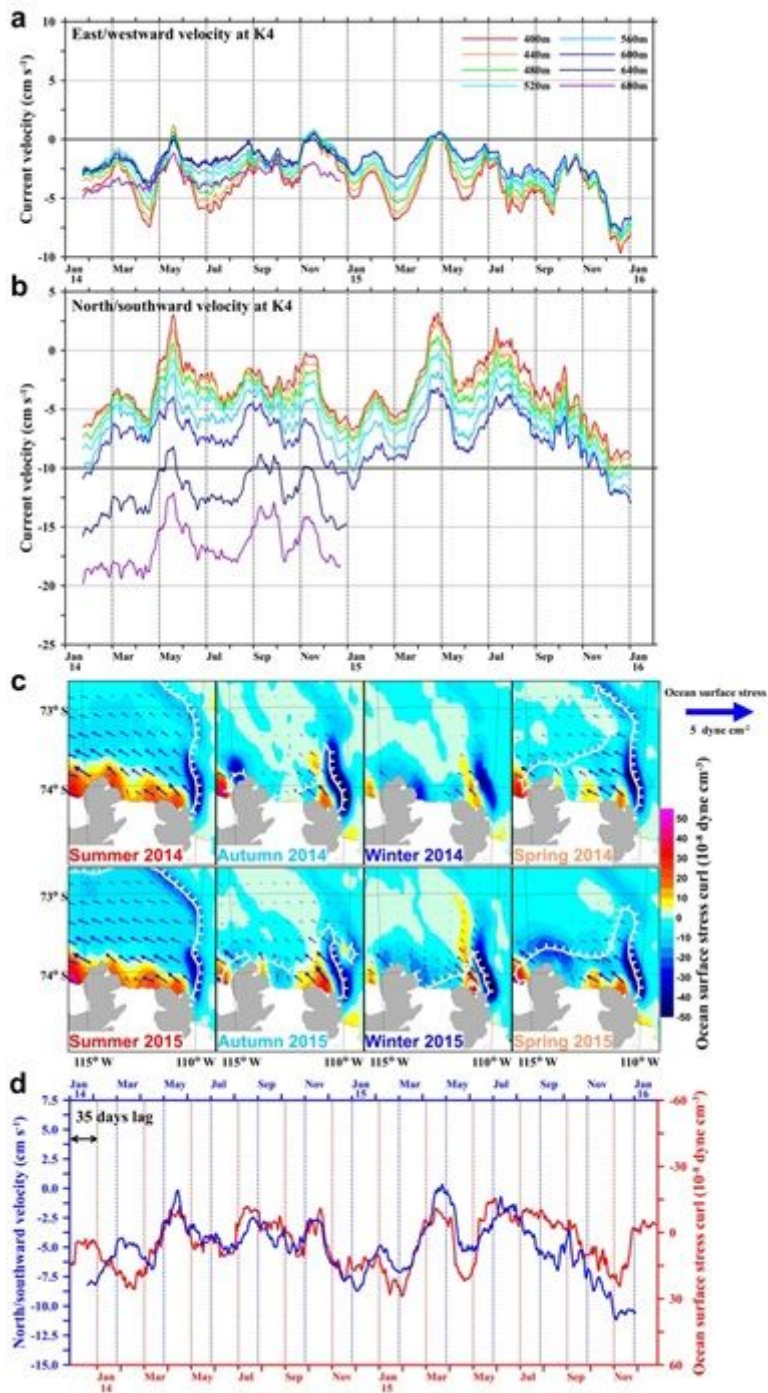


Figure 2

Time series of velocities and ocean surface stress curl. (a & b) 31 day running average zonal and meridional velocities at K4. Positive value is east and northward current. (c) horizontal distribution of ocean surface stress curl (color), ocean surface stress (arrow) and sea ice concentration (SIC) in 2014 and 2015. Uphill side of white hatched line indicates where SIC is over 50%. A positive OSSC means high sea surface height. (d) 31day running average OSSC at 74°S, 112.25°W (red) and vertical mean (400–600 m) meridional velocity (blue). Lower x-axis is back-shifted by 35 days.

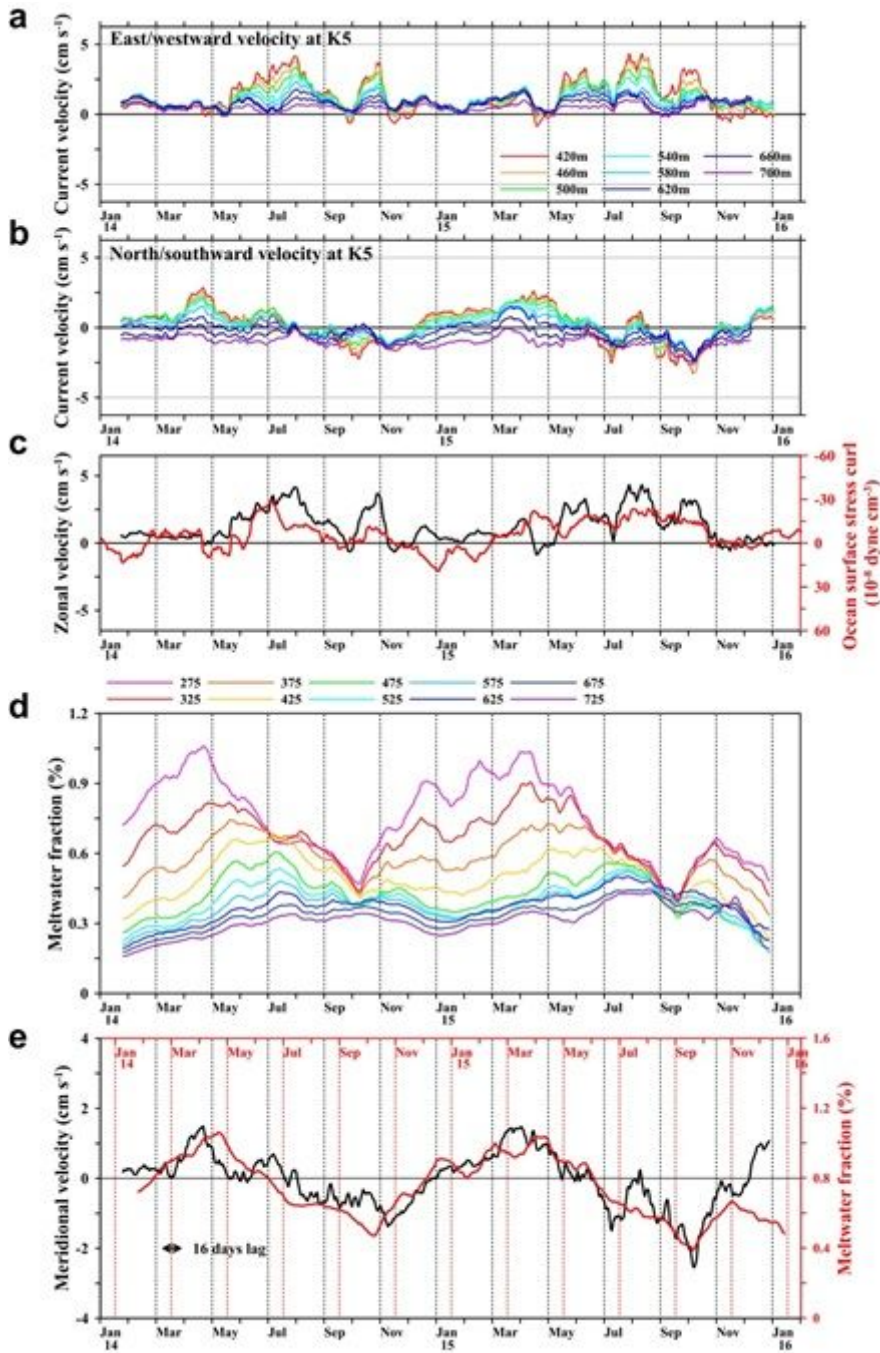


Figure 3

Time series of velocities and meltwater fraction at K5. (a & b) 31 day running average zonal and meridional velocities at K5. (c) 31 day running average zonal velocity (420m, black line) and mean OSSC (74°S, 112.75 - 113.25°W, red line). It showed a good correlation as $r = 0.57$. (d) 31 day running average meltwater fraction at 50 m intervals from 275–725 m (thin color-coded lines). (e) 31 day running average velocity (vertical mean, black line) and meltwater fraction (red line) at 275 m.

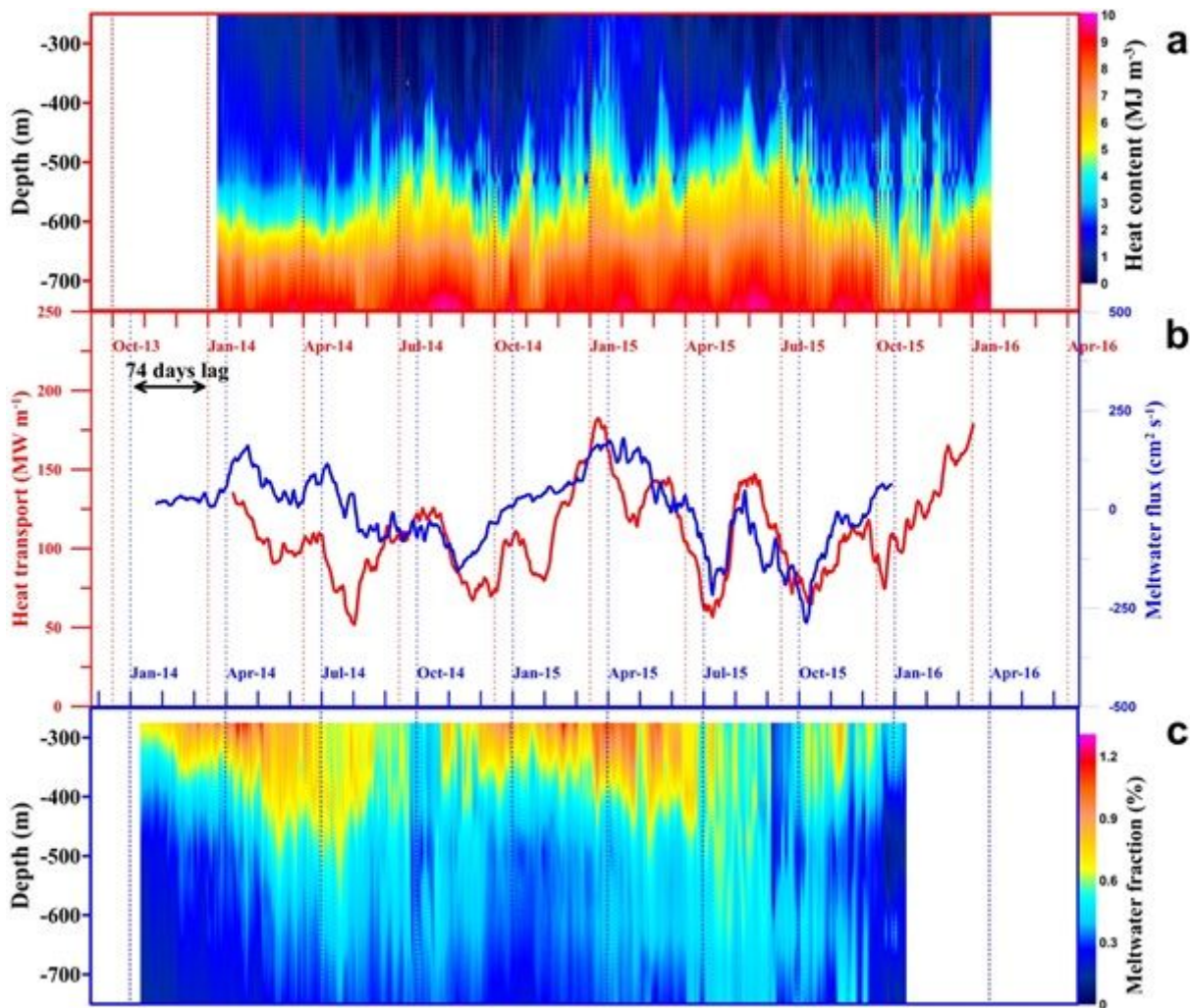


Figure 4

Time series of heat content and heat transport at K4 and meltwater fraction and meltwater flux at K5. (a) Vertical and temporal distribution of calculated heat content from 250–750 m at K4. (b) 31 day running average vertical mean meltwater flux(blue) between 275-575m at mooring K5 and estimated heat transport (red) at mooring K4. The upper x-axis for heat transport and content has been back-shifted 74 days. (c) Vertical and temporal distribution of meltwater fraction at mooring K5.

Supplementary Files

This is a list of supplementary files associated with this preprint. Click to download.

- [SupplementaryMaterials.pdf](#)